Check for updates

TECHNICAL REPORT

Establishing the ground squirrel as a superb model for retinal ganglion cell disorders and optic neuropathies

Xuan Xiao[1], Tantai Zhao[2], Kiyoharu J. Miyagishima [3], Shan Chen[3], Wei Li [3✉] and Francisco M. Nadal-Nicolás [3✉]

Retinal ganglion cell (RGC) death occurs after optic nerve injury due to acute trauma or chronic degenerative conditions such as optic neuropathies (e.g., glaucoma). Currently, there are no effective therapies to prevent permanent vision loss resulting from RGC death, underlining the need for research on the pathogenesis of RGC disorders. Modeling human RGC/optic nerve diseases in non-human primates is ideal because of their similarity to humans, but has practical limitations including high cost and ethical considerations. In addition, many retinal degenerative disorders are age-related making the study in primate models prohibitively slow. For these reasons, mice and rats are commonly used to model RGC injuries. However, as nocturnal mammals, these rodents have retinal structures that differ from primates - possessing less than one-tenth of the RGCs found in the primate retina. Here we report the diurnal thirteen-lined ground squirrel (TLGS) as an alternative model. Compared to other rodent models, the number and distribution of RGCs in the TLGS retina are closer to primates. The TLGS retina possesses ~600,000 RGCs with the highest density along the equatorial retina matching the location of the highest cone density (visual streak). TLGS and primate retinas also share a similar interlocking pattern between RGC axons and astrocyte processes in the retina nerve fiber layer (RNFL). In addition, using TLGS we establish a new partial optic nerve injury model that precisely controls the extent of injury while sparing a portion of the retina as an ideal internal control for investigating the pathophysiology of axon degeneration and RGC death. Moreover, in vivo optical coherence tomography (OCT) imaging and ex vivo microscopic examinations of the retina in optic nerve injured TLGS confirm RGC loss precedes proximal axon degeneration, recapitulating human pathology. Thus, the TLGS retina is an excellent model, for translational research in neurodegeneration and therapeutic neuroprotection.

INTRODUCTION

The retina, a layered light-sensitive tissue located in the back of the eye, is essential for vision and is an extension of the central nervous system (CNS). Photoreceptors convert light into electrical signals that are eventually transmitted to retinal ganglion cells (RGCs), which in turn convey the information to the brain for both image forming and non-image forming functions (such as circadian photoentrainment and pupillary reflex [1]). In the retina, most of the RGCs are situated in the ganglion cell layer (GCL), also known as orthotopic RGC (oRGCs), while a small proportion are located in the inner nuclear layer (INL), termed displaced RGC (dRGCs) [2–5]. Axons from both oRGCs and dRGCs form the optic nerve (ON) connecting the eye to the higher visual centers in the brain [6]. RGC axonal damage originating from optic nerve trauma or degeneration may lead to irreversible vision loss as mammalian CNS neurons normally cannot regenerate [7]. The eyes provide ease of access for surgical manipulation to model various human diseases [8–13]. Therefore, the retina (specifically RGCs) are often used to investigate degeneration of ganglion cells and their nerve fiber layers, neuronal survival, and axonal regeneration in the CNS. Traumatic ON injury (e.g., optic nerve crush, ONC) is a well characterized axonal injury and

neurodegenerative model that induces progressive RGC death [14–20]. Although RGC death is generally quantified ex-vivo, in vivo imaging directly through the optic media of the eye using spectral-domain optical coherence tomography (SD-OCT) confers an unique advantage to follow the progression of different retinal pathologies [21–25].

Rodents, such as mice and rats, are the most commonly used experimental mammals because they share basic retinal structure with the human retina and genomic information and genetic tools are readily available. However, these rodents are mostly nocturnal mammals with a rod-dominant retina [26, 27] and there are prominent structural differences compared to primate retina. Notably, the number of RGCs in these rodents are ten times lower than primate retina [28–30], reflecting a more primitive visual system focusing on rod vision. In contrast, the thirteen lined-ground squirrel (TLGS; *Ictidomys tridecemlineatus*) is a diurnal mammal with a cone-dominant retina [31–33]. Like most terrestrials mammals, TLGS possess two types of cones (M- and S-cones [31, 34–38]), whereas many primates (including humans) are trichromatic (L-, M- and S-cones [39–41]). Although the primate retina is in general rod-dominated (~95% rods [42]), its fovea region consists of cones and has a distribution pattern

[1]Eye Center, Renmin Hospital, Wuhan University, Wuhan, China; National Eye Institute, National Institutes of Health, Bethesda, MD, USA. [2]Department of Ophthalmology The Second Xiang-Ya Hospital; Central South University, Changsha, China; National Institutes of Health, Bethesda, MD, USA. [3]Retinal Neurophysiology Section, National Eye Institute, National Institutes of Health, Bethesda, MD, USA. ✉email: liwei2@nei.nih.gov; nadalnicolasfm@nih.gov

similar to the TLGS retina [31, 33]. Such a high density cone mosaic is likely associated with complex visual information carried by RGCs to the brain, and as a result, TLGS also have larger and highly developed visual areas in the brain compared to mice and rats [43].

TLGSs use their superior visual ability to navigate during the day, avoid predators, and forage for food [43]. In addition, the TLGS is an obligatory hibernator, surviving a lengthy period of winter by drastically reducing body temperature and suppressing metabolic need [32, 44, 45]. Thus, the TLGS is becoming an increasingly attractive model to study retinal disease associated pathology and the metabolic adaptative pathways as potential therapeutic targets [32, 33, 46, 47]. Previous studies have quantified RGCs or RGC axons in California ground squirrels [48, 49]. However, a more direct and complete depiction of the RGCs and associated cells in the TLGS is warranted given that it is currently the main ground squirrel species used in labs. We hypothesized that due to similarities in the overall number and density of retinal ganglion cells in TLGS and primate retina, the TLGS may have RGC and retinal nerve fiber layer (RNFL) structures that more closely resembled primates than other rodents. Thus, the optic nerve injury model in TLGS is valuable because it better recapitulates injuries and degeneration in human optic neuropathies. A characterization of RGCs and other cells in the ganglion cell layer (GCL) of the TLGS retina under normal/healthy and optic nerve injury conditions can therefore provide a foundation for further disease studies.

MATERIAL AND METHODS
Animal handling, anesthesia, and analgesia
Adult thirteen-lined ground squirrels (*Ictidomys tridecemlineatus*, hence TLGS, ~200 g, $n = 25$ squirrels) were obtained from a breeding colony at the University of Wisconsin Oshkosh. Three-month-old female pigmented mice (C57BL/6 J, $n = 6$ eyes) were obtained from the National Eye Institute (NEI) breeding colony. Postmortem eyes from nine-month-old female albino rats (Sprague Dawley, $n = 6$ eyes) were obtained from Dr. Tao Sun from the National Institute of Neurological Disorders and Stroke (NINDS). Postmortem eyes from eight to twelve-month-old Rhesus macaque (*Macaca mulatta*, $n = 4$ eyes) were obtained from Dr. Lauren Brinster from the Diagnostic and Research Services Branch of the NIH, Dr. Mark A. Eldridge from the National Institute of Mental Health and, Dr. Julie Mattison and Dr. Kielee Jennings from the Nonhuman Primate Core of the National Institute on Aging.

Mice were housed in a temperature and light controlled room with 12-hour light/dark cycles at 22 °C having free access to food and water. TLGS were similarly housed under these conditions during spring and summer seasons, but were placed into a hibernaculum at 5 °C beginning in the fall and housed throughout the winter as recommended [50]. Each species was treated and maintained according to their unique protocols (mouse, ASP#606; TLGS, ASP#595) approved by the National Institutes of Health guidelines for Animal Care and Use Committee in research and by the Ethical and Animal Studies Committee of the National Eye Institute. All animal studies conformed to the Statement for the Use of Animals in Ophthalmic and Vision research of the Association for Research in Vision and Ophthalmology (ARVO). In conducting this research, we adhered to the laws of the United States and regulations of the US Department of Agriculture.

Animals undergoing OCT imaging or surgery were anesthetized by isoflurane inhalation (Fluriso, Vet One, United Kingdom) and a drop of 0.5% proparacaine hydrochloride (Apexa, Akorn Pharmaceuticals Inc, Lake Forest, IL, USA) was provided as topical eye surface anesthesia. Eyes were kept hydrated with artificial tears (Systane Ultra, Novartis, Alcon) to prevent corneal desiccation and to maintain moisture and clarity.

Brain injection
To trace retinofugal projecting RGCs, we performed stereotactic injections of Fluorogold (3 µl, 6% diluted in 10% DMSO-saline) into both optic tracts as previously described for rats [51] one week prior to collecting and processing the tissues ($n = 4$ retinas). The coordinates of the optic tract in TLGS (+6 mm rosto-caudal, ±5 mm medio-lateral, and −6.5 mm

dorso-ventral from Lambda) were obtained using the "stereotaxic atlas of the brain of the 13-Line ground squirrel" [52].

Optic nerve injury
Due to the fact that squirrel eyes are set deeply into the eye sockets than those of mice and rats [32, 53], we adapted the standard optic nerve crush (ONC) techniques in rodents [18, 19] to TLGS. Briefly, the animal was placed on a heating pad during the surgery. After opening the conjunctiva along the supraorbital rim, the superior rectus muscle was dissected from its cranial portion preserving the scleral insertion (Fig. 1A). Tracking gently on this muscle allowed the eye to rotate exposing the optic nerve head (ONH). Holding the muscle, the meninges were longitudinally opened with micro-scissors to avoid damaging the blood vessels (Fig. 1A). After the ON was exposed, it was crushed for 10 sec with watchmaker's forceps. For the total ONC (tONC), the right ON was intraorbitally crushed ~2 mm from the center of the optic disc where in the TLGS all the axons converge together. For the partial ONC (pONC) only the nasal branch was crushed at a similar distance (Fig. 1B, C). Retinal ischemia was ruled out by fundus examination. Immediately after surgery, long-acting Meloxicam (Zoopharm, DRV Pharmacy NIH, 4 mg/kg) was provided by subcutaneous administration for analgesia and, the animal was transferred to an individual cage during the recovering period. For the tONC group the left eyes were used as controls, while the temporal halves in the pONC were used as internal control.

Retinal thickness measurements in vivo
TLGS eyes were scanned using SD-OCT (Spectralis; Heidelberg Engineering, Heidelberg, Germany). In both eyes a drop of tropicamide (Tropicamide Ophthalmic Solution, Akorn Pharmaceuticals Inc, Lake Forest, IL, USA) was instilled to induce iris mydriasis. To allow for comparison, we first characterized the retina nerve fiber layer (RNFL), ganglion cell complex (GCC) and retinal thickness along the eye fundus in intact animals ($n = 4$ retinas). The centro-nasal retina was scanned using 3×2 consecutive areas along the ONH. Each of these areas consisted of 31 equally spaced horizontal B-scans of 25 raster scan sequences [24, 25]. Each scanned area was ~3000 µm in length. The RNFL, GCC, and the retinal thickness were delineated manually and measured automatically to generate thickness maps per the manufacturer's instructions (Eye Explorer, v.1.10.0.0; Heidelberg Engineering). The resulting partial images were exported and edited in Photoshop (Photoshop 21.2.4; Adobe Systems, Inc.) to reconstruct the 3×2 thickness maps. Once the retinal thickness was characterized in intact uninjured animals, we selected an equidistant area from the ONH to allow comparison among retinas before and after ON injury (pONC or tONC). We averaged tree equidistant measurements in the 10th b-scan below the ONH for evaluation of retinal, RNFL, and GGC thickness (see scheme in Fig. 6A).

Tissue preparation
TLGSs and mice were euthanized by CO_2, while rat and monkey eyes were collected postmortem. TLGS and mice were perfused transcardially with 0.9% saline solution and immediately were perfused with 4% paraformaldehyde in 0.1 M phosphate buffer. Rat and monkey eyes were submerged in the same fixative solution for 1 h. To preserve retinal orientation, before enucleating the eyes, a burn point was placed in the dorsal pole. Immediately after eye enucleation, the retinas were carefully isolated from the eyecup and flattened as whole-mounts by making four (mice and rats) or eight (TLGSs and monkey) radial cuts. Then the retinas were mounted onto a filter membrane (HABP; Millipore, Bedford, MA, USA) and fixed in 4% paraformaldehyde in 0.1 M phosphate buffer for 1 h to maintain them flat. For classifying the GCL, a set of TLGS eye cups ($n = 3$), were embedded in paraffin, sectioned by microtome at 3 µm thickness and subjected to hematoxylin-eosin staining. Another set of eye cups (mice, $n = 3$; rat, $n = 3$; TLGS, $n = 5$; monkey, $n = 2$) and optic nerves were cryoprotected in a graded sucrose series (Sigma, #84097) and embedded in optimal cutting temperature (Sakura Finetek, Torrance, CA, USA) at −80 °C for cryo-sectioning (Leica, CM3050S) at 16 µm thickness. All retinal cross sections were done following the dorso-ventral (DV) axis and comprised both the superior and the inferior retina. Sections containing longitudinal blood vessels were excluded from our retinal evaluations.

Immunofluorescence
RGCs were identified in cross sections and in whole-mount retinas by immunodetection using two RGC-specific proteins, Brn3a [18] (Brain-specific homeobox/POU domain protein 3 A) and RBPMs [54, 55] (RNA-binding
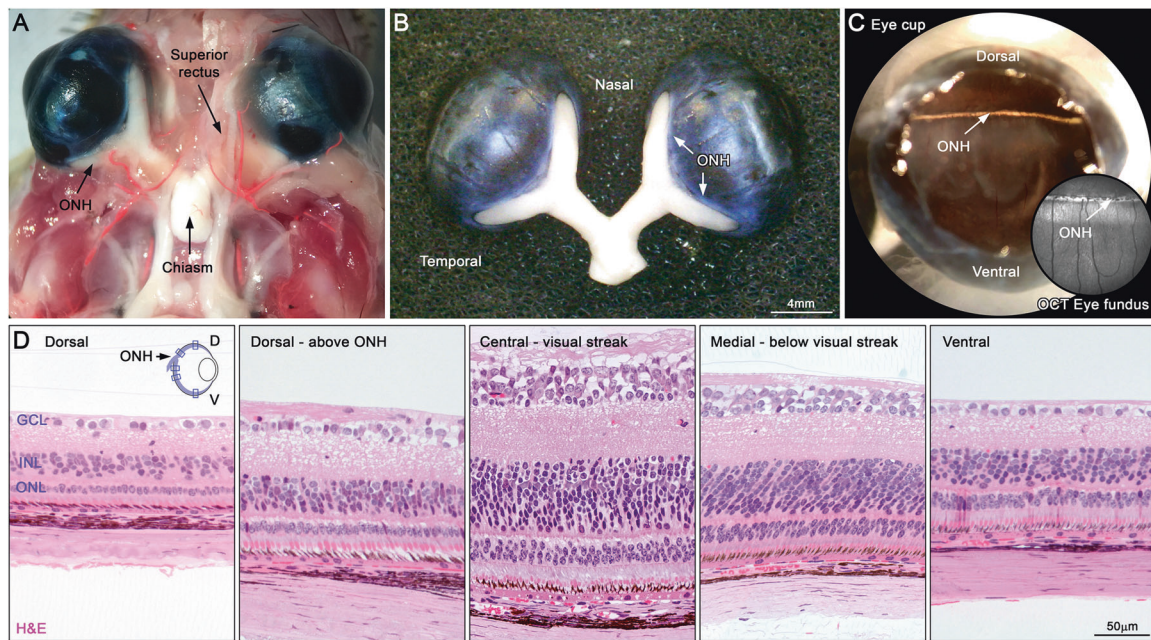
Fig. 1 Ocular and retinal anatomy of thirteen-lined ground squirrel. A Anatomy of the proximal visual pathway of thirteen-lined ground squirrel (TLGS). The ocular globes, optic nerves, and optic chiasm are exposed. The dorsal skull and the superior rectus muscle were removed (in the left eye) to allow visualization of the optic nerve head (ONH) and the retinal arteries (untouched during the surgery procedure). **B** Dorsal image of the ocular globes and optic nerves after enucleation. The retinal ganglion cells axons extend out from the ocular globe through a linear ONH. Approximately 1.5 millimeters away they merge forming the distinctive 'Y'-shape. **C** Internal view of the TLGS eye cup, after removing the cornea and lens, showing the posterior pole of the vitreous chamber and the ONH placed above the equatorial region and extending horizontally for several millimeters [53]. (**C**, right bottom) Eye fundus of TLGS acquired in vivo by the SD-OCT showing the ONH and the retinal vasculature. **D** Retinal cross sections stained with hematoxylin-eosin (H&E) in different retinal areas along the dorsoventral axis (DV, scheme in **D**). Note that the rows of nuclei in the ganglion cell layer (GCL) increases towards the central retina, while in the periphery the GCL constitutes a monolayer. *INL* inner nuclear layer, *ONL* outer nuclear layer.

protein with multiple splicing) diluted at 1:500. Subpopulations of amacrine cells were detected using different antibodies; ChAT (Anti-Choline Acetyl-transferase), glycine, GAD65 + 67 [56] (Glutamic Acid Decarboxylase) or calretinin diluted at 1:250. Astrocytes (GFAP, Glial fibrillary acid protein) and Microglial cells [20] (MCs; Iba1, Ionized calcium-binding adapter molecule 1) were also immunodetected (1:1000) to characterize the GCL composition. The ON sections were additionally immunolabeled for CD68 to identify activated MCs (1:1000). Whole-mount retinas were also immunolabeled for neurofilament heavy phosphorylated (pNFH) [16, 57] and cleaved caspase-3 (c-Casp3) [58] diluted at 1:500 to characterize the RGC and axonal degeneration after ON injury. Complete antibody information is described in Supplementary Table S1A. The antibody specificity on TLGS tissue was confirmed by the high homology among the protein sequences across different species (*Homo sapiens, Macaca fascicularis, Ictidomys tridecemlineatus, Rattus norvegicus, Mus musculus*; detailed in Supplementary Table S1B). Briefly, all retinas were permeabilized in PBS 0.5% Triton X100 four times (10 min each). Retinas were then incubated for six days with the primary antibody in blocking buffer (2% Normal Donkey Serum, 0.5% Triton X100 in PBS) at 4 °C. Afterwards the retinas were washed and incubated for two days with the proper secondary antibodies diluted 1:500. Finally, retinas were thoroughly washed in PBS and cover-slipped vitreal side up with antifading mounting medium with DAPI (4',6-diamidino-2-phenylindole, ThermoFisher, D1306) to counterstain all nuclei.

Image acquisition

Retinal sections, optic nerve sections, and whole mounted retinas were analyzed under a confocal microscope (Zeiss Z1 - LSM 780, Zeiss microscopes) equipped with a computer-driven motorized stage controlled by its own image analysis software (Zen Lite Back edition 2012, Zeiss). The retinal and optic nerve photomontages were reconstructed using the maximum projection of individual images (20x) by zig-zag tiling with an overlap of 8% between frames. To characterize the GCL composition, images of retinal sections (20x) were acquired at three different retinal areas (periphery, medial and central or visual streak). However, to uncover the whole retina surface, magnifications from flat mounts retinas (63x) were acquired in five regions along the DV axis

(dorsal periphery, above ONH, visual streak, medial retina and ventral periphery; 4 images/region) using the same settings.

Ganglion cell layer characterization in TLGSs

To characterize the RGC population in TLGSs we evaluated the expression of different antibodies against RGC, amacrine cells (ACs), astrocyte and microglial cells (MCs) in retinal cross sections. Neuronal markers were quantified manually in the GCL, while glial markers were also measured in the adjacent layers; the RNFL and the inner plexiform layer (IPL). The different populations were characterized per retinal area (periphery, medial and central retina) and by their specific location in the GCL.

Automatic quantification. Brn3a+ orthotopic-RGC and DAPI+nuclei

To develop an automatic algorithm to quantify Brn3a+oRGCs, 30 samples were taken from different retinal areas (6 samples/retina, $n = 5$ retinas). Brn3a+nuclei (RGCs) were automatically quantified on whole-mount retinas using a macro developed using ImageJ (Supplementary File S1). Briefly, to minimize interference with background labeling, a rolling ball radius of 50 pixels was subtracted. Then, all images were transformed into 8-bit grayscale to discard color information followed by the application of a predetermined lower threshold to extract positive edges from the dark background and create a binary mask-like image. Next, "watershed" segmentation automatically separates particles that touch and "despeckle" median filter removes the noise. Last, positive objects were counted within fixed parameters (shape and size) to exclude objects that were too small or too large to be considered nuclei. Finally, the routine automatically extracts the number of counted objects and their x, y position coordinates. All data were exported to a spreadsheet (Office Excel 365; Microsoft Corp.) for further analysis ($n = 11$ retinas). This automated routine was validated by statistical comparison with manual quantifications carried out by an experienced investigator (Pearson correlation coefficient $R^2 = 97\%$; 69,378 cells were quantified manually while 63,021 were obtained automatically). To quantify the number of RGCs in the central retina, a 3 mm diameter area was obtained from the center of the retinal photomontage (~1.5 mm

below the ONH) in intact and after tONC, while it was extracted from the nasal portion after pONC. Minimal adjustments (threshold and object size) were performed to adapt this routine to quantify DAPI$^+$nuclei in whole ON sections or at the injury site (longitudinal area of 1×0.2 mm centered in the injury site).

Manual quantification. Brn3a$^+$ displaced-RGCs and Iba1$^+$cells

After the whole retinas were photographed, the dRGCs were detected by changing the microscope focus from the GCL to the inner nuclear layer. dRGCs were manually dotted in the retinal photomontage ($n = 12$ retinas) using a photoediting program (Photoshop 21.2.4; Adobe Systems, Inc) as previously reported [5]. The Iba1$^+$cells were also manually dotted directly on the ON photomontage. The number of dots and the position coordinates representing each dRGC or Iba1$^+$cell, were automatically obtained using the ImageJ software. Finally, all the data including the spatial coordinates and number of dots were exported to a spreadsheet (Microsoft Office Excel; Microsoft Corp., Redmond, WA, USA) for spatial analysis (see next section). In addition, to examine the number of Iba1$^+$cells in the injury site, we extracted the same area described above (1×0.2 mm) after completing the manual dotting.

Spatial topography

The numerical coordinates (x, y) from each Brn3a$^+$RGCs were obtained from the whole retinal photomontage. These data were exported to a spreadsheet application (Microsoft Office Excel) to assess the spatial distribution by calculating the number of neighbors per RGCs using a fixed radius (70 μm for oRGCs and, 345 μm for dRGC) as previously described [5]. However, the density of DAPI$^+$nuclei and Iba1$^+$cells in the ONs were evaluated by 83.3×83.3 μm areas. Both type of values where plotted using a graphics editing program (SigmaPlot 13.0 for Windows; Systat Software, Inc., Richmond, CA, USA) to show the k-neighbor or isodensity maps as described previously for other rodent species [17–20, 25]. To further characterize the distribution of RGCs along the retinal surface, we divided the retina along the two main axes: dorsoventral and temporonasal (DV, TN, respectively). The oRGC ($n = 11$ retinas) were assessed in an 6 mm width for the DV profile, and 6 mm high for the TN profile to prevent misplaced reads due to the radial cuts for flattening the retina, while dRGC ($n = 12$ retinas) where assessed in the whole surface. The RGC profiles are represented in line graphs (mean ± standard deviation; SigmaPlot 13.0).

Nuclear area

The nuclear area of Brn3a+oRGCs was measured in five retinal regions (135×135 μm, 63x) at different eccentricities. Two samples were taken in the dorsal retina, peripheral and medial (above the optic disc), and the other three areas corresponded to the inferior retina (visual streak, medial, and peripheral). For the visual streak two images were acquired, one in the most superficial row (~1–10 μm deep) and the other subsequently deeper (~15–25 μm deep). To simplify the graph representation, we averaged both peripheral (from dorsal and ventral) and both medial measurements because no significant differences were observed after analyzing the results. We measured a total of 13,544 Brn3a$^+$nuclei ($n = 6$ retinas) plotted as the percentage of cells per nuclear area at different eccentricities.

Statistical analysis

Data representation and comparisons among all data sets were carried out with a statistical software package (GraphPad Prism v.8, GraphPad San Diego, CA, USA). D'Agostino test was used to analyze the normal distribution of all data sets. Cellular quantifications or thickness measurements were analyzed by multiple comparison one-way ANOVA and Tukey's test for post-hoc analysis. The sample size for the different studies was detailed in the corresponding tables. Data are presented as mean ± standard deviation (SD) and differences were considered significant when $p < 0.05$ (*), $p < 0.01$ (**), or $p < 0.001$ (***).

RESULTS

Characterization of the ganglion cell layer in TLGS

The TLGS eyeball is asymmetric along the DV axis, with a linear optic nerve dividing the smaller dorsal and larger ventral portion [59] (roughly 1:2). In the peripheral retina, hematoxylin/eosin staining showed that the GCL is composed of a monolayer of nuclei but increased to four rows in the central retina (Fig. 1D).

Knowing that not all the nuclei in the GCL belong to the RGC, we used two reliable and widely used RGC markers, Brn3a [18] and RBPMs [54, 55] to identify RGCs. In cryostat cross sections, signals from Brn3a and RBPMs antibodies were largely co-expressed in the GCL, and the RGC population represented ~49% of the DAPI$^+$ nuclei in the GCL (Fig. 2A–A', Supplementary Table S3A). Towards the central retina, the proportion of RGCs in the GCL increased to 57% (Fig. 2A', Supplementary Table S2A–B). Notably, the expression of both RGC markers was notably reduced in the outer row of the GCL in the middle and central retina (Fig. 2A–A', horizontal histograms). To examine whether those non-RGCs in the outer row of the GCL belong to the dAC, we used a set of antibodies (ChAT, glycine, GAD65 + 67, and calretinin). Indeed, the ChAT$^+$dACs were situated almost exclusively in the outer most GCL-row of the medial retina, or in the two outer most layers in the central retina (Fig. 2B–B'). Glycine and GAD65 + 67 positive cells showed a similar pattern, while calretinin detected a subpopulation of dACs and RGCs (Fig. 2C), as previously reported [60], expanding across the GCL. We further assessed the non-neuronal populations, astrocytes (GFAP) and microglial cells (MCs, Iba1) in the GCL. Astrocyte somas were mainly restricted to the RNFL along the retinal surface with a few embedded into the most inner GCL-row (Fig. 2D–D', Supplementary Table S2C). Similarly, the MCs were largely absent from the GCL in resting conditions, located mainly in the IPL and a few in the RNFL (Fig. 2D–D', Supplementary Table S2C). This arrangement was not obvious in mouse and rat retinas, since their GCL is a constant monolayer across the entire retina (Fig. 2E–F). However, examining macaque cryo-sectioned retinas revealed a similar pattern to TLGS retinas, with even more numerous RGC-rows and fewer ChAT$^+$dACs in the central retina (Fig. 2G).

Additional characterization of the visual streak in flat mount retinas corroborated this GCL distribution. Within three sublayers of GCL (inner, middle, and outer), the RGCs (RBPMs$^+$Brn3a$^+$ + RBPMs$^+$Brn3a$^-$) were highly concentrated in the inner and middle layers (87.3%, 52.9%, and 11%, inner, middle, and outer, respectively, Fig. 3A–A', Supplementary Table S3), while the ChAT$^+$dACs and Glycine$^+$ and were mostly placed in the outer layer (41.2% and 26.2% ChAT and Glycine, respectively, Fig. 3B–C, B'–C', Supplementary Table S3), confirming the results from cross sections (Fig. 2). Among RBPMs$^+$RGCs, Brn3a$^-$ subpopulation represent a small fraction (5.4 in retinal sections and 4.3% in flat-mount retinas respectively, Fig. 3D–E, Supplementary Table S4), and were slightly more concentrated in the dorsal retina (Fig. 3E, Supplementary Table S4) and towards the inner most GCL-row of the central retina (Fig. 2A', Supplementary Table S4).

Number and topography of RGCs in TLGS

To examine the number and distribution of the RGC population across the whole retina in the TLGS we employed two different techniques that both identified a high-density region along the equatorial retina below the ONH. This area corresponds to the visual streak region [31]. In the first technique, retrograde tracing by injecting Fluorogold into the optic tracts, identified a majority of the RGCs with brain-projecting axons. High-magnification images along the DV axis showed the different RGC densities across the retina (Fig. 4A). In the second technique, Brn3a immunolabeling confirmed this RGC distribution and allowed for a more precise quantification of RGCs by the use of an automated algorithm (for details see "Material and Methods"). Within the GCL, the population of Brn3a$^+$oRGCs averages ~600,000 (594,815 ± 37,407, $n = 11$, Fig. 4B, Table 1A), while displaced RGCs are scarce (319.9 ± 38, $n = 12$, Fig. 4C, Table 1A), representing only the 0.054% of the total population. The k-neighbor maps of the distribution of oRGCs across the entire retina (Fig. 4B) show lower RGC density in the dorsal retina, whereas the ventral retina exhibited an increasing gradient from the periphery toward the
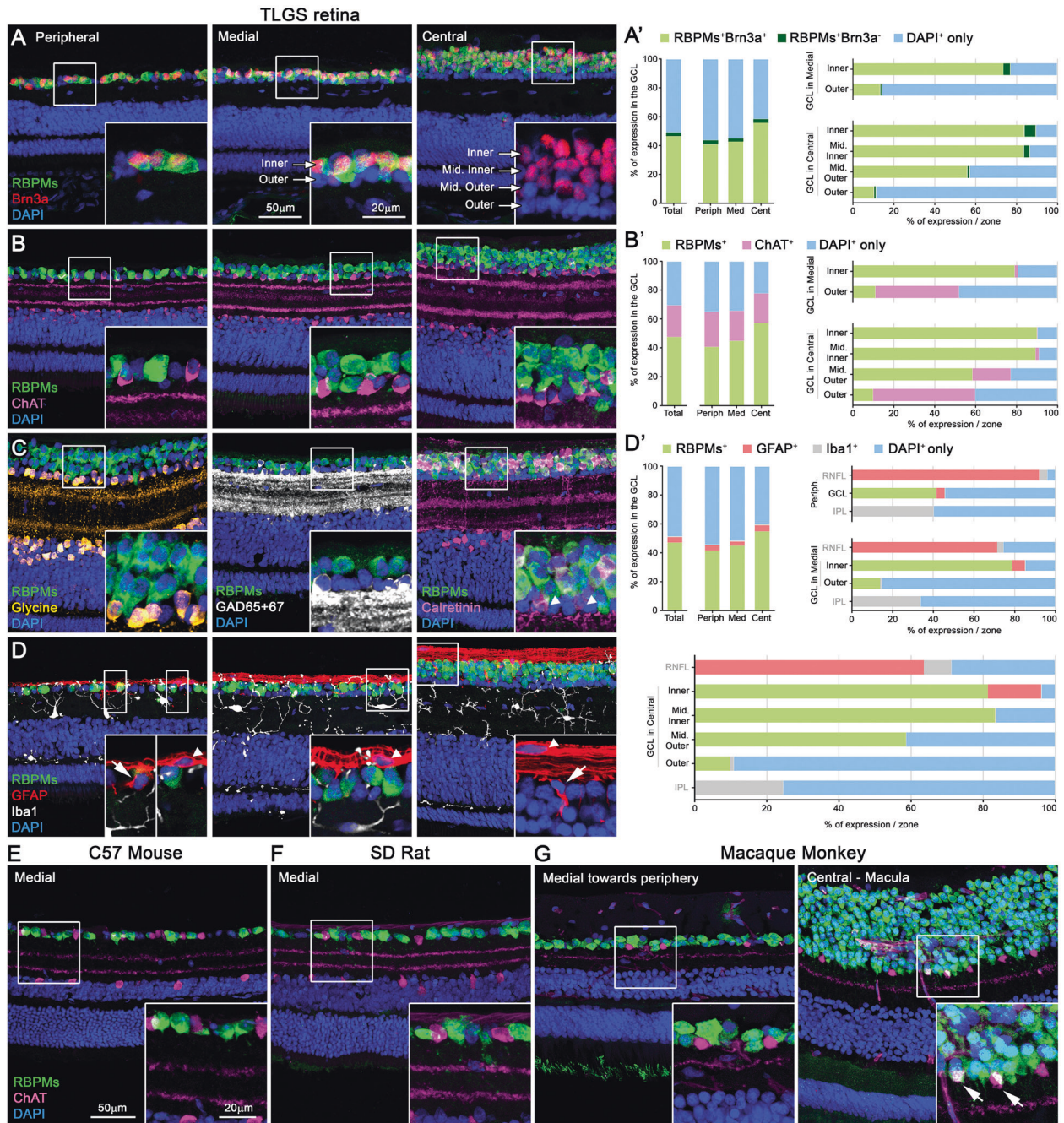
Fig. 2 **Characterization of ganglion cell layer in thirteen-lined ground squirrel retinal sections. A** Retinal cross sections of TLGS retinas along the dorsoventral axis (DV, from peripheral, medial and central retina) stained with antibodies against various retinal cell types. **A–A′** Identification and quantification of RGCs in the ganglion cell layer (GCL) using Brn3a and RBPMs antibodies counterstained with DAPI. In the medial and central retina, the RGCs were located mainly in the inner most rows of the GCL. **B** Expression of ChAT⁺displaced amacrine cells (dACs) in the GCL. Note that in medial and central retina the ChAT⁺dACs were confined mostly to the outer GCL rows. Quantifications of ChAT⁺dACs and RBPMs⁺RGCs along the DV axis are shown in (**B′**). **C** Identification of other dACs populations by glycine, GAD65 + 67, or calretinin immunodetection in combination with the RGC detection (RBPMs) to corroborate their specific location into the GCL assembly. **D** Identification and quantification of astrocytes and microglial cells (MCs) in the GCL and the surrounding retinal layers (retinal nerve fiber layer, RNFL and inner plexiform layer, IPL). Note that details in (**D**) correspond to a single-plane images. Vertical histograms show the percentage of RGCs (co-expressing RBPMs⁺Brn3a⁺ or RBPMs⁺Brn3a⁻, **A′**), ChAT⁺dACs (**B′**) or astrocytes and MCs (**D′**) in overall (total), at different retinal areas (peripheral, medial and central), while horizontal histograms depict each cell-type contribution to the different GCL-rows in the medial and central retina (from inner to outer GCL-rows). **D′** Astrocytes and MCs estimations include the retinal nerve fiber layer (RNFL) and the inner plexiform layer (IPL) where they are predominantly found. **E–G** Retinal cross section from mouse (C57BL/6 J), rat (Sprague-Dawley) and Rhesus macaque immunostained with RBPMs and ChAT antibodies to label the GCL pattern. The GCL extended as a monolayer along the whole retina surface in mouse and rat retinas (**E–F**), however, the macaque displayed a gradual increase in the number of rows towards the central retina (**G**) similar to the TLGS retina (**B**). This distinct pattern of RGC somas stacked over multiple layers is exaggerated in the macula of the primate retina. The RGCs occupy most of the rows in the GCL and the few ChAT⁺dACs are confined to the outer row (**G**). Note that in two cases the ChAT⁺dACs are overlapping RBPMs⁺RGCs (Arrows in **G**).
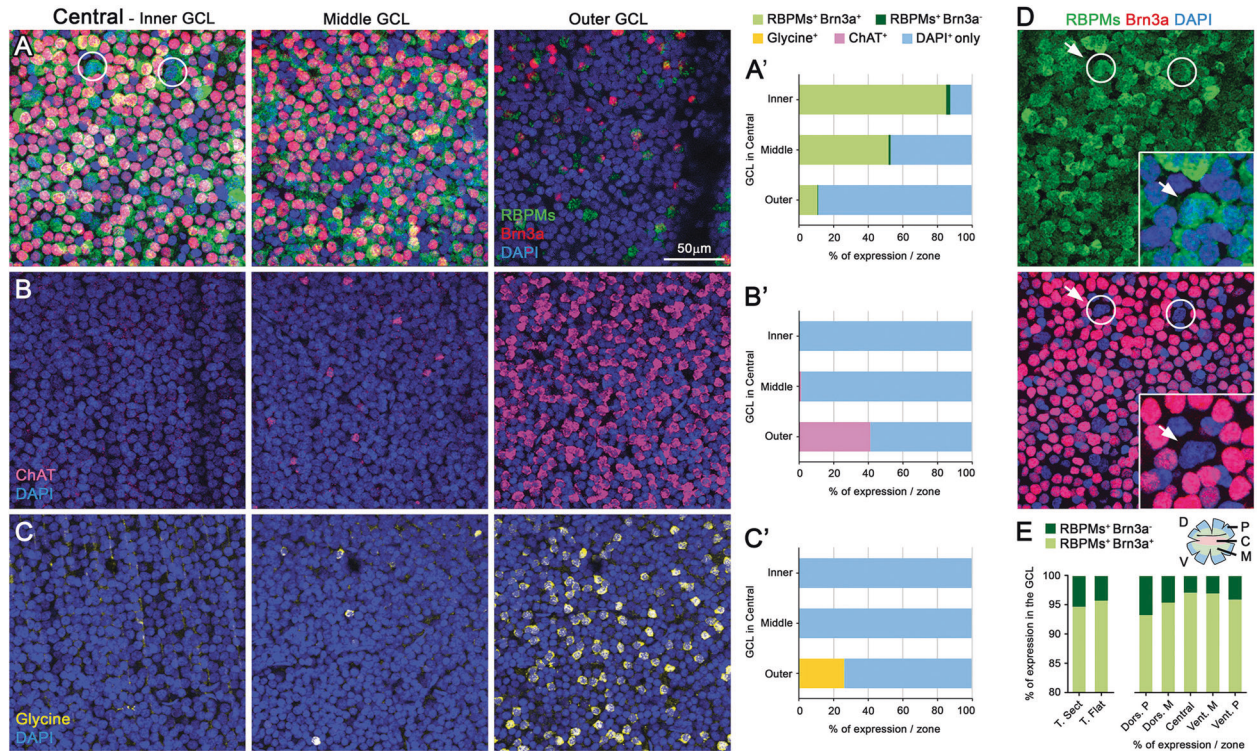
Fig. 3 Characterization of the ganglion cell layer in thirteen-lined ground squirrel flattened retinas. Immunodetection of Brn3a and RBPMs (RGCs, **A**), ChAT or glycine (dACs, **B**, **C**, respectively) counterstained with DAPI at three different focus planes of the same area in flat-mounted TLGS retinas. **A'–C'** Horizontal histograms depict the percentages of RGC (Brn3a$^+$ and RBPMs$^+$), ChAT$^+$dACs or Glycine$^+$dACs per zone of the GCL in central retina. These results corroborate the observations described in the retinal section analysis (Fig. 2). **D** Images of Brn3a and RBPMs co-expressing RGCs in retinal flat-mounts (same area as in **A**). The circles depict RBPMs$^+$Brn3a$^-$RGCs. **E** Vertical histogram showing the percentage of RBPMs$^+$Brn3a$^-$RGCs in retinal sections (total), flat retinas (total) or along the DV axis (by distinguishing five retinal areas: dorsal periphery, above optic nerve head, visual streak, medial retina, and ventral periphery, see retinal scheme in **E**). RBPMs$^+$Brn3a$^-$RGCs are slightly concentrated in the dorsal retina.

central retina. The highest oRGC density was at the visual streak in the equatorial retina ~1 mm below the ONH (Fig. 4B). Parallel analysis from the same retinas revealed that dRGCs also concentrated in the visual streak beneath the ONH and, with a much smaller peak above the ONH that diffusely spread towards the dorso-temporal region. Evaluating the distribution of RGCs in the DV and TN axis confirmed such distribution profiles (Fig. 4D). Both the densities of oRGCs and dRGCs are slightly more towards the temporal retina (Fig. 4D) with peak densities found in the visual streak, but the dRGCs show a much narrower distribution around the visual streak.

In addition, using Brn3a as a nuclear marker, we observed that the size of RGC nuclei varies according to their location, with bigger nuclei in the periphery. Further analysis of the central retina by layers revealed that RGC nuclei were even smaller in deeper layers of the GCL (Fig. 4E).
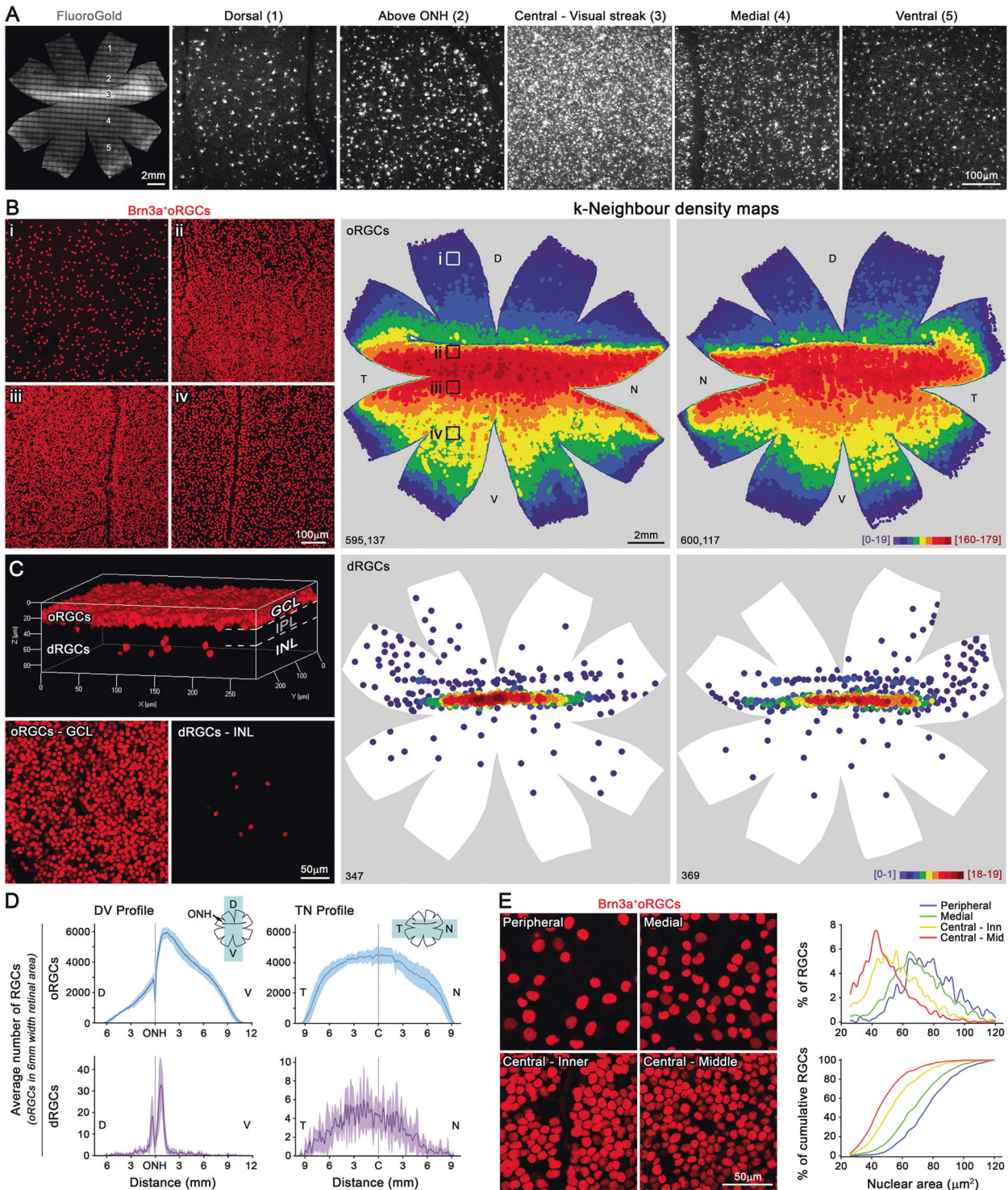
Optic nerve crush and glial response
Aiming to use TLGS to study RGC degeneration, we have performed two injury paradigms, pONC and tONC. In intact optic nerves, astrocyte dendrites have parallel orientation to the ganglion cell axons, sending short processes transversally to organize the axons in bundles as described for mice [61]. MCs under typical resting conditions showed a ramified morphology without CD68 (MC activation marker) expression and were evenly distributed throughout the entire ON (Fig. 5A, a). At 14 days after injury, we noticed dramatic changes in the glial cells. We observed an absence of astrocytes in the injury site and those at the outskirt showed a reactive, hypertrophic morphology, with some out-crossing appendages into the damaged area (Fig. 5B–C, b–c).

Meanwhile, MCs exhibited vigorous activation along the ON and a subpopulation of MCs selectively amassed at the injury site. In fact, these MCs had an ameboid or round shape and co-labeled with CD68 (Fig. 5b–c).

After pONC, in the whole ON there was an increase in cellular density (DAPI$^+$ nuclei) compared to intact optic nerves (111%, Fig. 5D–E first row, Table 1B). After tONC, a further increase in cell density (126%) was found compared to pONC. We observed a similar trend when analyzing the MC density in the whole ON but with an even higher percentage of increase (180%, Fig. 5D–E second row, Table 1B). Despite these observed differences in cell and MC density in the whole ON following pONC or tONC, when we focused solely on the injury site, we observed similar numbers of DAPI$^+$ cells and MC densities for both ONC models (Fig. 5F, Table 1B). This result indicates that cellular responses to ONC are relatively restricted to the injury site regardless of the size of the crush.

SD-OCT measurements and RNFL anatomy
To examine the degeneration of RGCs and their axons after ONC, we characterized the thickness of different retinal layers along the nasal portion of the dorso-central retina using the ONH as reference (scheme shown in Fig. 6A). This extensive examination of the eye fundus allows for comparison of the same retinal area post injury among animals at various time points. Thus, we manually delineated the retinal, GCC, and the RNFL thickness from the same intact retinas. In agreement with the density maps of RGCs, we observed that the visual streak is the thickest region of the retina (Fig. 6B). However, the RNFL was thicker from the superior border of the visual streak toward the ONH, indicating

A FluoroGold | Dorsal (1) | Above ONH (2) | Central - Visual streak (3) | Medial (4) | Ventral (5)

B Brn3a⁺oRGCs — k-Neighbour density maps

oRGCs

595,137 · 600,117 · [0-19] [160-179]

C oRGCs — dRGCs

oRGCs - GCL · dRGCs - INL

347 · 369 · [0-1] [18-19]

D DV Profile · TN Profile

E Brn3a⁺oRGCs — Peripheral, Medial, Central - Inner, Central - Middle

that this area contains a higher number of axons (Fig. 6D). Interestingly, the GCC was thicker in the area comprising the visual streak up to the ONH, likely due to a thicker RNFL (Fig. 6C). Therefore, to perform reliable comparisons among animals and after ON injury, we selected an area 1 mm ventral below the ONH (Fig. 6A).

The first significant thinning following ONC was observed at 14 days measuring the GCC (83% and 82.3%, pONC and tONC, respectively), and RNFL thickness (75.4% and 79.3%, pONC and tONC, respectively, Fig. 6E–F, Table 1C), but the retinal thickness was not statistically different among groups (Fig. 6E–F, Table 1C). As expected, we did not observe significant differences between partial or total ONC since we always measured the nasal (injured-side, pONC) or injured retina (Fig. 6E–F).

To examine the detailed cellular structure of the RNFL in TLGS and to compare it with other animal model species, we performed ex vivo antibody labeling of pNFH⁺, which labeled RGC axons in the RNFL uniformly and showed axon bundles running parallel towards the ONH, similar to axon bundles in the mouse, rat, and primate retina (Fig. 6G–J). However, in mouse and rat retinas,

Fig. 4 Retinal ganglion cells topography and visual field of thirteen-lined ground squirrel. A Flattened whole-mount retina of TLGS traced with Fluorogold (FG) from the optic tracts. The FG-labeling revealed high concentration of RGCs in the visual streak. Magnifications show the different RGC densities along the DV axis at seven days after FG injection into the optic tracts. **B** Microphotographs of RGCs labeled with Brn3a along the DV axis and topographic maps of Brn3a⁺ orthotopic RGCs (oRGCs) in TLGS. Magnifications of representative different Brn3a⁺oRGC density to areas selected by frames in the adjacent map (i, ii, iii, iv). The k-neighbor maps were reconstructed from flat whole-dissected retinas depicting the distribution of oRGCs in three dimensions (x, y, and color scale). **C** Lateral view of a 3D reconstruction from a z-stack containing oRGCs and displaced RGCs (dRGCs) in the central retina. Flat images of individualized Brn3a⁺ oRGCs or dRGCs acquired at different focus planes (GCL and INL, respectively) in the 3D block. Topography of Brn3a⁺dRGCs in the INL in the same retinas analyzed for the oRGC topography. **B–C** The total number of Brn3a⁺RGCs counted in each retina are shown at the bottom of each map. K-neighbor maps representing the number of neighbors around each cell within a given radius visualized using a color scale. For oRGCs the color scale (neighbors/oRGC) is defined from 0–19 (purple) to 160–179 neighbors/oRGC (dark red), each color represents an increase of twenty neighbors in a radius of 70 μm; while the color scale for dRGCs is defined from 0–1 (purple) to 16–17 neighbors/dRGC (dark red), each color represents an increase of two neighbors in a radius of 345 μm. **D** RGC profiles in the dorsoventral and temporonasal axis (DV and TN, respectively). Line plots depict the average of oRGCs and dRGCs (Y axes) at increasing distances from the ONH (X axes, in mm). Note that both oRGC and dRGC populations peak in the visual streak (from 1 to 2.5 mm below the ONH), and the temporal retina contains slightly more RGCs than the nasal counterpart. **E** Different RGC-nuclear areas (μm²) along the retinal surface. Line plots showing the averaged or the cumulative distribution of the Brn3a⁺RGC-nuclei size at four different retinal locations. D dorsal, T temporal, V ventral, N nasal.

astrocytes displayed typical star-shape morphology, wrapping the blood vessels and contacting axon bundles as they traverse through them (Fig. 6G–H). In contrast, the astrocyte processes in TLGS are bundled in parallel with and form close contacts along the RGC axons (Fig. 6I). Essentially, RGC axons in TLGS appear to be shielded by astrocyte processes. Interestingly, such relationship between RGC axons and astrocytes processes is remarkably similar to that of the primate retina (Fig. 6J), indicating that TLGS could potentially be a more faithful disease model of optic neuropathies in the context of neuron-glia interaction.

Retinal ganglion cell degeneration after traumatic optic nerve injury

To characterize the RGC degeneration after ONC in TLGS retinas we performed triple immunolabeling of (i) Brn3a to identify surviving RGCs, (ii) cleaved-Caspase3 (c-Casp3) to detect apoptotic RGCs, and (iii) pNFH to reveal the status of the degenerating RGC and axons. As reported previously, pNFH is normally expressed in axons (Fig. 7A–a), however, it starts to accumulate abnormally in the soma as a symptom of degenerating and dysfunctional RGCs (Fig. 7B–b, C, arrow), or in the form of rosary beads along the axons [16] (Fig. 7C, arrowhead). Analyzing the c-Casp3 expression at 14 days, we observed apoptotic RGCs in the far-middle retina (Fig. 7B). Although, Brn3a expression is greatly reduced in most apoptotic RGCs [58, 62], we identified a few RGCs in an intermediate state of degeneration as their soma contain: (i) accumulation of neurofilament, (ii) expression of c-Casp3, (iii) a weak Brn3a signal, corroborating that they are indeed dying RGCs (details in Fig. 7b). Those moribund cell bodies eventually disappear, leaving an axonal stump that withdraws from the vanishing soma (a sequence shown in Fig. 7C'–C"). Further investigation in the transition zone after pONC show a clear view of both scenarios. As described previously, the c-Caps3 expression is restricted to the crushed site of the retina where most of the Brn3a⁺RGCs are missing and the loss of RGC axons are evident in the central retina at 14 days post injury. (Fig. 7D).

After both forms of ON injury, the RGC loss was significant at fourteen days (276,608 ± 60,486, n = 7 and 73,886 ± 29,927, n = 6, pONC and tONC, respectively, Fig. 7E, Table 1A) compared with intact retinas (594,815 ± 37,407, Fig. 4B). K-neighbor maps of surviving RGCs showed a diffuse loss of Brn3a⁺ oRGCs either affecting the nasal retina after pONC or the entire retina after tONC (Fig. 7F). The RGC loss quantified for the whole retina was more pronounced after tONC than pONC, reflecting the extent of injury (12.4% and 46.5%, respectively, Fig. 7F, Table 1A). However, the degeneration in both cases followed a similar rate. The RGC survival in the central retina (3 mm Ø within the injury area) showed a similar RGC survival rate after pONC and tONC (9.5% and 8.1%, respectively, Fig. 7F, Table 1A). In addition, after both

pONC and tONC, the RGC loss was higher in the central retina than in the peripheral, as described in the rat retina [19, 20]. Note that at 14 days after tONC, on average 12.4% of total RGCs survived, while the survival rate is only 8.1% in the central area (Fig. 7G).

DISCUSSION

Our main objective in the present manuscript was to characterize the anatomical features of the RGC population and their axons under healthy control and injured conditions in order to establish the TLGS as an animal model for studying RGC degenerative diseases. First, we characterized the GCL in control retinas and discovered that the RGCs are not randomly mixed with dACs but organized in the inner rows of the GCL. Second, we quantified the entire population of RGCs in whole-mount retinas, demonstrating a spatial distribution of high density RGCs in the visual streak area matching that of the cone photoreceptors [31]. Third, we characterized the RGC degeneration following ONC and found the course and degenerative patterns are similar to other species such as mice [17, 58], rats [18–20, 24], goat [63] and monkey [64], indicating a conserved pathological process that can be exploited to model human conditions. Last, we highlighted anatomical differences, between TLGS and other rodents, revealing TLGS retinas to be more similar to primate retina, indicating that the TLGS is a potentially more faithful model for human RGC diseases.

Retinal ganglion cells in the GCL of TLGS

Like other rodents, the GCL of the TLGS retina is composed of a mixture of RGCs, dACs, and a small fraction of non-neuronal cells [19, 65]. One key feature of the TLGS retina is the high concentration of RGCs in the central retina, with as many as four layers of RGCs making up ~60% of the cells in GCL (compared to 40% in rat retina [19]). Although not as high as in the central primate retina [29, 66–69] (up to 97% of GCL cells), such multi-layered RGC distribution is closer in resemblance to the central primate retina, compared to other rodents which usually only have a single layer of RGC cells throughout the retina. This likely reflects the cone-dominant nature of the TLGS retina conveying more visual information than nocturnal rodents [48]. Indeed, the high density RGC area corresponds to the visual streak defined by the highest density of cones [31].

Furthermore, the RGCs are mainly restricted to the inner rows of the GCL, while different subpopulations of dACs (ChAT, glycine, GAD65 + 76, calretinin) situate in the outer most row. This particular layout may reflect the temporal sequence of neurogenesis during development – RGCs are among the earliest to differentiate and occupy the apical layers of the GCL [70, 71], and dACs which originate later and thus have to settle in the outer layer of the GCL. Anatomically, it could also facilitate RGCs to send

Table 1. Cellular densities, total cell number, and thickness of the thirteen-lined ground squirrel retina and optic nerve in intact and after partial or total ONC.

A. Neuronal population in whole mount retinas

Cell type	Staining	Area	Intact (oRGC $n = 11$, dRGC $n = 12$)	pONC 14 d ($n = 7$)	tONC 14 d ($n = 6$)
RGCs	Brn3a$^+$oRGC	Whole retina	594,815 ± 37,407	276,608 ± 60,486 (46.5%)	73,886 ± 29,927 (12.4%)
		3 mm Ø	44,513 ± 3469	4,218 ± 2,643 (9.5%)	3,622 ± 2,274 (8.1%)
	Brn3a$^+$dRGC	Whole retina	319.9 ± 38 (0.054%)		

B. Cellular and microglial populations in whole-optic nerve sections and in the injury site.

Cell type	Staining	Area	Intact ($n = 5$)	pONC 14 d ($n = 7$)	tONC 14 d ($n = 3$)
All	DAPI	Whole ON	2,653.4 ± 75.5	2,938.3 ± 113.7 (111%)	3,348.5 ± 55.7 (126%)
		Injury site (1 × 0.2 mm)	2,880.3 ± 164	7,264 ± 985.2 (252%)	6,826 ± 1,588.2 (237%)
Microglia	Iba1$^+$MCs	Whole ON	250.6 ± 19.2	450.8 ± 62 (180%)	664 ± 68.5 (267%)
		Injury site (1 × 0.2 mm)	276.2 ± 15.4	2,804 ± 361.2 (1015%)	2,843 ± 111.1 (1029%)

C. In vivo thickness measurements (µm)

Zone	Measure	Intact ($n = 10$)	pONC 7 d ($n = 7$)	tONC 7 d ($n = 3$)	pONC 14 d ($n = 7$)	tONC 14 d ($n = 3$)
Central	Retina	240.2 ± 15	236 ± 19 (98.3%)	243.7 ± 12.2 (101.4%)	223.3 ± 20.4 (92.9%)	224.2 ± 5.7 (93.3%)
	GCC	131.4 ± 5	124.7 ± 8 (95%)	128.7 ± 9.3 (98%)	109 ± 10.6 (83%)	108.2 ± 1.4 (82.3%)
	RNFL	36.3 ± 2	36.4 ± 4 (100%)	37.4 ± 4.3 (103%)	27.4 ± 3.4 (75.4%)	28.8 ± 2.5 (79.3%)

(A) Total number of Brn3a$^+$oRGCs in the GCL and Brn3a$^+$dRGCs in the INL. (B) Number of DAPI$^+$nuclei and Iba1$^+$cells in cryosectioned optic nerve in TLGS. (C) In vivo thickness of the retina, ganglion cell complex (GCC) and retina nerve fiber layer (RNFL) in the TLGS.

their axon into the RNFL, which is adjacent to the inner GCL layer. We also found that the size of RGC nuclei (Brn3a$^+$ labeling) is larger in the inner layer than those found in the outer layer – in accordance with the gradual dwindling of available space for developmental late-comers. Such a stereotypical layout of RGCs in the GCL is conserved in the primate retina (Fig. 2G) but is obviously missing in the mouse and rat retina, owing to their monolayer of RGCs.

Among RBPMs$^+$ RGCs, ~96% are Brn3a$^+$ (Supplementary Table S4), in agreement with previous reports for other rodents [5, 17, 18, 62]. The remaining RBPMs$^+$/Brn3a$^-$ RGCs are slightly more concentrated in the dorsal retina. Those cells likely include the intrinsically photosensitive RGCs (ipRGCs) since they do not express Brn3a as reported previously [1, 62]. Although some poly-axonal amacrine cells may also be RBPMs$^+$/Brn3a$^-$ [55], they rarely reach the inner layer of GCL. Thus, these putative ipRGCs are situated at a front-row location without much light scattering from retinal tissues which would be beneficial for global light detection.

Number and topography of RGCs in TLGS
We quantified Brn3a$^+$ RGCs in the TLGS retina to be ~600,000 (Table 1A). This number is likely to be slightly underestimated for two reasons. First, we chose Brn3a over RBPMs antibody for quantification because nuclei labeling (Brn3a) is easier to segregate and quantify than soma labeling (RBPMs). However, there are ~4% of RGCs that are Brn3a negative. Second, although we obtained a high precision in our automatic RGC-counting algorithm compared with manual counting ($R^2 = 97\%$), the RGC number is likely underestimated in the central retina ($R^2 = 79\%$), owing to the limitation of 2D image-based quantification that may miss some RGCs in the visual streak where there are multiple layers of RGCs. However, even with these considerations, the total number of RGCs remains lower than the previous quantification of California ground squirrel

optic nerve that provided an estimation of ~1.2 million axons [49]. This discrepancy can perhaps be attributed to species difference and unknown numbers of centrifugal axons that were not excluded in the California ground squirrel study [49], nonetheless the number appears to be high, considering that primate/human retinas which have a much larger retina and higher RGC density in the central area have only about ~1.3 million RGCs [28–30]. Regardless, ground squirrels seem to have RGC numbers that are closer to primates and humans, and are much higher than other rodent models (~15 and ~7 times more than mouse and rat retinas respectively [5, 17, 18, 58]).

Although lacking a fovea structure, the visual streak in TLGS retina has a peak RGC density (close to 10,000 RGCs/mm^2) on par with the peri-fovea region of the primate retina [67], presumably representing an area with high visual acuity. This is similar to previous report on California ground squirrels [48] (24,000 nuclei/mm^2, assuming 50% of which are RGCs). We verified this RGC distribution pattern by retrograde labeling of Fluorogold injection into the optic tract [51]. This method is superior than the commonly practiced SC injection in other rodents, as the SC in TLGS is much bigger [43, 52], thus requiring multiple injections to cover most of the RGC projections. Interestingly, dRGCs also sharply concentrate in the same region slightly extending toward the temporal quadrant. In the mouse retina, dRGC neurogenesis is under the control of Glycogen Synthase Kinase 3 and may contribute to binocular vision as they project to the ipsilateral thalamus [72, 73]. The functional role of dRGCs in TLGS remains to be explored.

Optic nerve crush and glial response
Although partial ON injury has been performed in other species [64, 74], the TLGS retina is particularly suitable owing to its linear, 'Y'-shape optic nerve head that permits injury to half of the axons with an ideal internal control from the uninjured half.
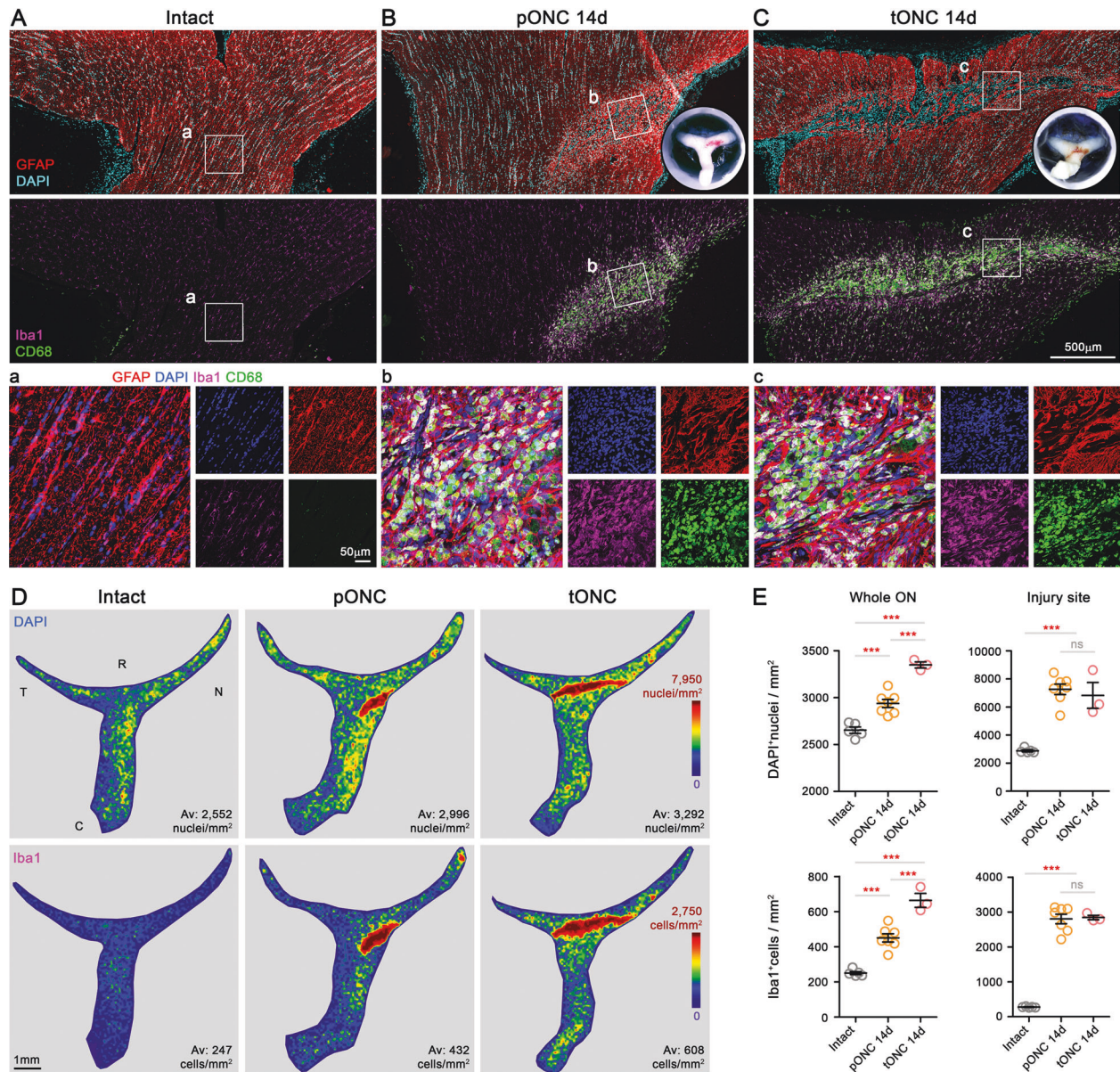
Fig. 5 Optic nerves after traumatic injury in thirteen-lined ground squirrel. Magnified images from representative horizontally sectioned ON showing astrocytes (GFAP) counterstained with DAPI (**A**, first row), or microglial cells (MCs, Iba1) and MC activation (CD68) in intact (**A**, second row), at 14 days post pONC (**B**) or post tONC (**C**). Details of the injury site showing the crush-length after partial or total ONC (**B–C**, first row, right bottom). **A** The surveying MCs were distributed homogeneously along the optic nerve (**a**), while the activated microglia-like cells were highly concentrated and numerous in the injury site after optic nerve damage (**B–C**). Details show the similar appearance of the glial scar at 14 d after pONC and tONC (b and c, respectively). **D** Isodensity maps depict the distribution of DAPI$^+$nuclei or Iba1$^+$MCs whole ON sections from intact, at 14 d after pONC or tONC. Color scale defined from 0 DAPI$^+$nuclei/mm^2 (purple) to 7950 DAPI$^+$nuclei/mm^2 (red), or from 0 Iba1$^+$MCs/mm^2 (purple) to 2750 Iba1$^+$MCs/mm^2 (red). The number of quantified cells in the corresponding ON are shown below each map. **E** Plots showing the mean density (±SD) of DAPI$^+$nuclei and Iba1$^+$MCs in whole ON or in the injury site (1 × 0.2 mm area) in intact or at 14 d post ONC. d days, R rostral, C caudal, T temporal, N nasal.

Importantly, the level of RGC death, glia cell accumulation, and pattern of cellular responses appeared to be comparable between pONC and tONC at 14 days post injury. There is not a significant spread of injury-induced pathology towards the uninjured half. The key feature of the lesion is the accumulation of activated MCs in the center of the lesion surrounded by hypertrophic astrocytes. This is different from the mouse spinal cord injury [75–77], in which newly proliferated scar-forming astrocytes grow into the injury site. It is generally believed that MCs are mainly participating in the inflammatory response and phagocytosis of axonal debris [78], whereas the glial scar

formation depends on the astrocyte-microglia interactions [79]. Recent results [80, 81] have challenged the old dogma of glial scar preventing axon injury recovery [82–84]. Thus, the implication of MC and astrocyte pattern observed here on RGC axon regeneration warrants further study. More time points post injury will be needed to capture the dynamics of glial responses.

In vivo SD-OCT measurements and ex vivo pathology
SD-OCT provides a valuable tool to detect structural changes in the retina and to follow injury progression. Although both the GCC
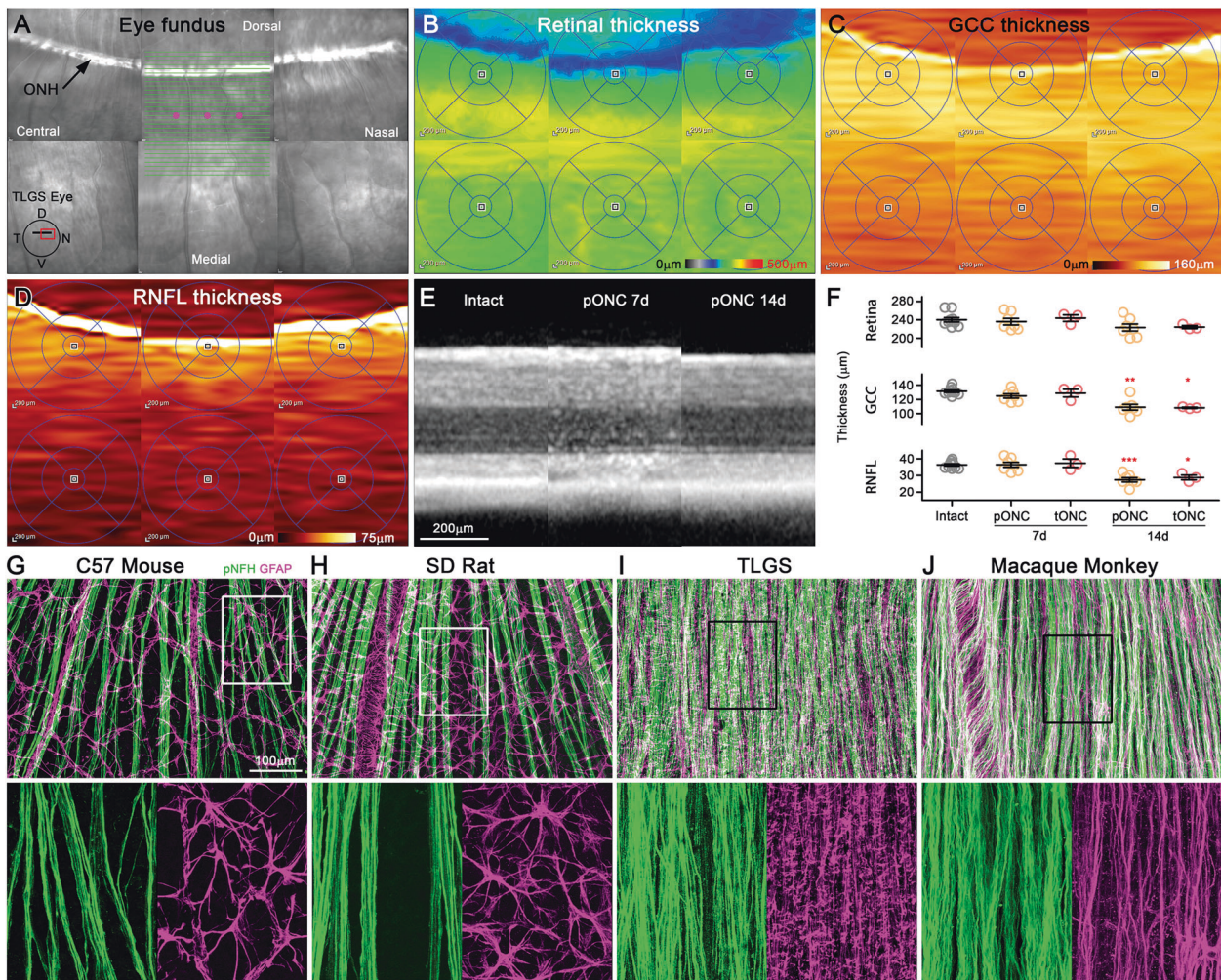
Fig. 6 **Retinal thickness evaluation in thirteen-lined ground squirrel. A** Representative example of the TLGS eye fundus reconstructed by 3 × 2 individual fundus images acquired in vivo from central toward nasal retina along the ONH by SD-OCT. The 3 × 2 scanned area corresponds to the red selected area in the TLGS eye schematic in the lower left panel of **A**. Note that the ONH of the TLGS runs horizontally along the central retina. Manual segmentation was performed to determine measurements of the whole retinal thickness (**B**), ganglion cell complex (GGC, **C**) and retinal nerve fiber layer (RNFL, **D**) thickness. **B–D** Representative images from OCT volume scan analysis for the retina (**B**), GCC (**C**) or RNFL (**D**) in intact TLGS retinas. **E** Representative sections from the B-scan were analyzed further using volumetric analysis of the central retina (1 mm below the visual streak, see schematic in **A**) obtained from the same eye at intact and post-surgical conditions (7 and 14 days post-ONC). **F** Volumetric analysis of the retina, GCC, or RNFL thickness showed no difference between partial or total ONC in the centro-nasal retina. After ONC, retina, GCC, and RNFH indicated no significative changes at 7 days but revealed significant thinning of the GCC and RNFL at 14 days post-injury. **G–J** Comparison of the RNFL and astrocyte interactions in different species including mice (**G**), rats (**H**), TLGSs (**I**) and monkeys (**J**). While astrocytes displayed typical star-shape morphology in mouse and rat retinas with punctual interactions with the RGC axons (**G–H**), they primarily "ensheathe" the axons in TLGS and monkey retinas (**I–J**).

and RNFL thickness declined significantly at 14 days after ONC, the RNFL thinning appeared milder, compared to the extent of RGC loss observed ex vivo. While the glial cell proliferation and infiltration [85–87] could contribute to the maintenance of the RNFL thickness, ex vivo immunolabeling revealed axons remain in injured retinal regions despite significant RGC loss (Fig. 7D–E) – indicating RGC loss precedes the RNFL and GCC thinning, as previously described in rat [24]. In addition, detailed analysis captured the sequence of cellular events underlying degeneration. Initially the degenerating soma exhibits decreased Brn3a expression and increased caspase 3 expression (Fig. 7A–B). This is followed by the accumulation of pNFH in the failing soma, and in later stages the dissolved soma leaves behind a "flare ending" of the retracting axon (Fig. 7C–C"). This process is likely not uniform across the retina, with the central retina leading the peripheral areas [19] (Fig. 7G) as a result of: (1) being closer to the injury site

[15]; (2) higher metabolic demand [88, 89]. Interestingly, we found in the RNFL of the TLGS retina, astrocyte dendrites form dense bundles and "ensheathe" the RGC axons, whereas such interactions are much looser in mouse and rat RNFL (Fig. 6G–H). This may also contribute to the different rate of degeneration as the peripheral RGC axons have longer segments covered by such astrocyte processes. This feature of astrocyte-axon interaction is also observed in the primate retina; thus, it would be interesting to study the impact of such neuro-glial interaction, especially in the context of axonal injury.

TLGS is a good model for RGC and optic nerve pathologies with features similar to primates
Overall, the TLGS confers several advantages as a model for studying RGC neurodegeneration and optic neuropathy. First, the TLGS is a diurnal rodent having a cone-dominated retina with a
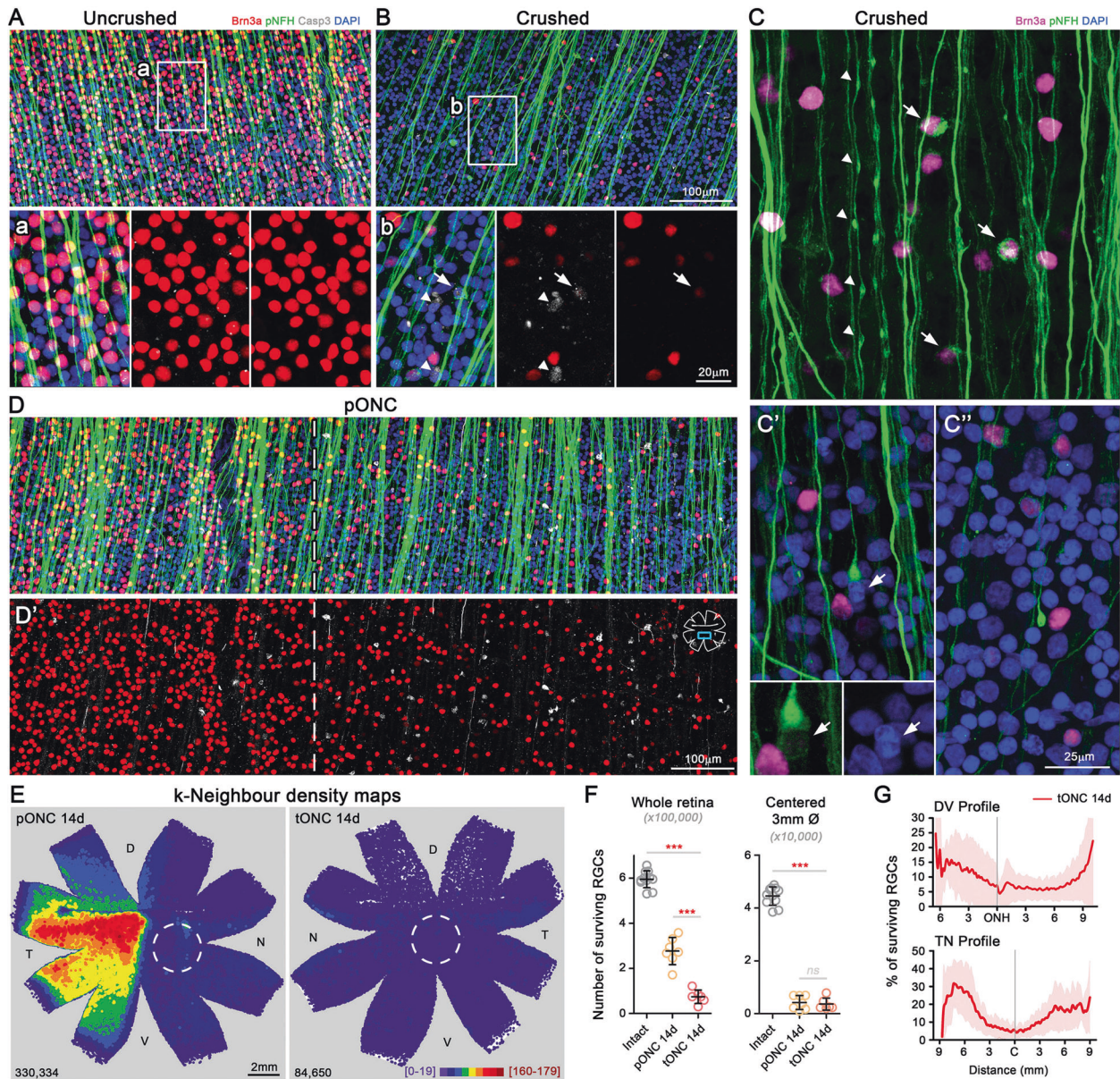
Fig. 7 Retinal ganglion cells loss after optic nerve crush in thirteen-lined ground squirrel. Magnified images from flat-mounted retinas taken from the mid-ventral retina. The surviving RGCs (Brn3a), apoptotic RGC (cleaved-Caspase 3) and the nerve fiber layer (pNFH) are shown in representative images of the uncrushed retinal portion (**A**), crushed (**B**–**C**) or the transition zone (**D**) in the same retina at 14 d post pONC. Details in a show typical RGC axons (pNFH) and the absence of apoptotic RGCs (cleaved-Caspase 3 expression) in uncrushed retinas. Details in (**b**) show loss of RGCs (Brn3a) and the appearance of apoptotic RGCs (c-Casp3+, arrowheads). Note a degenerating RGC in an intermediate state; somatic accumulation of neurofilament (pNFH), Casp3 expression and weak Brn3a signal (arrow). Details in (**C**) show typical alterations in the intraretinal axons, beaded axons (arrowheads, **C**), somatic accumulation (arrows, **C**), and the formation of axonal ending in flare-like shape (**C'**–**C''**). **D** The crushed half of the transition zone indicates a correlation between RGC loss and c-Casp3 expression at 14 d post pONC (area is shown in the upper right of **D'**). K-nearest neighbor maps reveal the extensive Brn3a+RGCs loss at 14 d post pONC or tONC. The total number of Brn3a+RGCs counted in each retina are shown at the bottom of each map. The number of neighbors was calculated used a radius of 70 μm and the neighbor maps were plotted using the same color scale descried for intact retinas (Fig. 4). **F** Plot showing the mean number (±SD) of surviving Brn3a+RGCs in whole retinas or in the central retina (3 mm diameter area) in intact or after ONC. **G** RGC profiles in the DV axis showing the average (±SD) surviving RGCs after tONC compared with intact retinas (Y axes) at increasing distances from the optic nerve head (X axes, in mm). d days, D dorsal, T temporal, V ventral, N nasal.

highly dense cone area known as the visual streak. Accordingly, multiple layers of RGCs are enriched in this area, with a density closely matching the primate perifoveal region. In addition, in the RNFL, the anatomical structure of astrocyte-RGC axon interaction closely resembles primates. Given the increasing evidence implicating the role of astrocytes in RGC death [90], this structural interaction will likely have a substantial impact on the

pathophysiological process of optic nerve injury and RGC loss. These primate-like features render it a good model for the human retina. Second, the unique optic nerve structure of TLGS makes it possible for reliable partial injury, offering a potential model to study secondary degeneration in axons spared from the initial injury and to have an internal control for experiments such as sequencing and treatments. Third, the TLGS is an obligatory

hibernator, therefore its metabolic flexibility may be exploited for strategies to deal with injury/disease-induced stress. Of course, being a non-model species and a hibernator, it has disadvantages compared to other rodents such as lower availability, higher cost, difficulty breeding, lack of genetic tools, seasonal food and handling requirements (individual housing, environmental enrichments, hibernaculum, etc) [50], however, it can be a complimentary model species bridging the gap between mice and primates.

DATA AVAILABILITY STATEMENT
The data that supports the findings of this study are available within the article and its supplementary material. Raw or additional data are available from the corresponding author upon reasonable request.

REFERENCES
1. Chen S-K, Badea TC, Hattar S. Photoentrainment and pupillary light reflex are mediated by distinct populations of ipRGCs. Nature. 2011;476:92–5.
2. Dogiel AS. Die Retina der Vögel. Archiv f mikrosk Anat. 1895;44:622–48.
3. Dräger UC, Olsen JF. Origins of crossed and uncrossed retinal projections in pigmented and albino mice. J Comp Neurol. 1980;191:383–412.
4. Doi M, Imatani H, Sasoh M, Uji Y, Yamamura H. Displaced retinal ganglion cells in the Chinese hamster. Jpn J Ophthalmol. 1994;38:139–43.
5. Nadal-Nicolás FM, Salinas-Navarro M, Jiménez-López M, Sobrado-Calvo P, Villegas-Pérez MP, Vidal-Sanz M, et al. Displaced retinal ganglion cells in albino and pigmented rats. Front Neuroanat. 2014;8:99.
6. Ramón y Cajal S. The Structure of the retina (compiled and translated by Thorpe SA, Glickstein M). Springfield, Ill. C.C. Thomas, 1972.
7. Case LC, Tessier-Lavigne M. Regeneration of the adult central nervous system. Curr Biol. 2005;15:749–53.
8. Salinas-Navarro M, Alarcón-Martínez L, Valiente-Soriano FJ, Jiménez-López M, Mayor-Torroglosa S, Avilés-Trigueros M, et al. Ocular hypertension impairs optic nerve axonal transport leading to progressive retinal ganglion cell degeneration. Exp Eye Res. 2010;90:168–83.
9. Vidal-Sanz M, Salinas-Navarro M, Nadal-Nicolás FM, Alarcón-Martínez L, Valiente-Soriano FJ, de Imperial JM, et al. Understanding glaucomatous damage: anatomical and functional data from ocular hypertensive rodent retinas. Prog Retin Eye Res. 2012;31:1–27.
10. Ortín-Martínez A, Salinas-Navarro M, Nadal-Nicolás FM, Jiménez-López M, Valiente-Soriano FJ, García-Ayuso D, et al. Laser-induced ocular hypertension in adult rats does not affect non-RGC neurons in the ganglion cell layer but results in protracted severe loss of cone-photoreceptors. Exp Eye Res. 2015;132:17–33.
11. García-Ayuso D, Salinas-Navarro M, Nadal-Nicolás FM, Ortín-Martínez A, Agudo-Barriuso M, Vidal-Sanz M, et al. Sectorial loss of retinal ganglion cells in inherited photoreceptor degeneration is due to RGC death. Br J Ophthalmol. 2014;98:396–401.
12. Zhang J, Li L, Huang H, Fang F, Webber HC, Zhuang P, et al. Silicone oil-induced ocular hypertension and glaucomatous neurodegeneration in mouse. Elife. 2019;8:45881.
13. Sappington RM, Carlson BJ, Crish SD, Calkins DJ. The microbead occlusion model: a paradigm for induced ocular hypertension in rats and mice. Invest Ophthalmol Vis Sci. 2010;51:207–16.
14. Misantone LJ, Gershenbaum M, Murray M. Viability of retinal ganglion cells after optic nerve crush in adult rats. J Neurocytol. 1984;13:449–65.
15. Villegas-Pérez MP, Vidal-Sanz M, Rasminsky M, Bray GM, Aguayo AJ. Rapid and protracted phases of retinal ganglion cell loss follow axotomy in the optic nerve of adult rats. J Neurobiol. 1993;24:23–36.
16. Parrilla-Reverter G, Agudo M, Nadal-Nicolás F, Alarcón-Martínez L, Jiménez-López M, Salinas-Navarro M, et al. Time-course of the retinal nerve fibre layer degeneration after complete intra-orbital optic nerve transection or crush: a comparative study. Vision Res. 2009;49:2808–25.
17. Galindo-Romero C, Avilés-Trigueros M, Jiménez-López M, Valiente-Soriano FJ, Salinas-Navarro M, Nadal-Nicolás F, et al. Axotomy-induced retinal ganglion cell death in adult mice: quantitative and topographic time course analyses. Exp Eye Res. 2011;92:377–87.
18. Nadal-Nicolás FM, Jiménez-López M, Sobrado-Calvo P, Nieto-López L, Cánovas-Martínez I, Salinas-Navarro M, et al. Brn3a as a marker of retinal ganglion cells: qualitative and quantitative time course studies in naive and optic nerve-injured retinas. Invest Ophthalmol Vis Sci. 2009;50:3860–8.
19. Nadal-Nicolás FM, Sobrado-Calvo P, Jiménez-López M, Vidal-Sanz M, Agudo-Barriuso M. Long-term effect of optic nerve axotomy on the retinal ganglion cell layer. Invest Ophthalmol Vis Sci. 2015;56:6095–112.
20. Nadal-Nicolás FM, Jiménez-López M, Salinas-Navarro M, Sobrado-Calvo P, Vidal-Sanz M, Agudo-Barriuso M. Microglial dynamics after axotomy-induced retinal ganglion cell death. J Neuroinflammation. 2017;14:218.
21. Choe TE, Abbott CJ, Piper C, Wang L, Fortune B. Comparison of longitudinal in vivo measurements of retinal nerve fiber layer thickness and retinal ganglion cell density after optic nerve transection in rat. PLoS ONE. 2014;9:e113011.
22. Liu Y, McDowell CM, Zhang Z, Tebow HE, Wordinger RJ, Clark AF. Monitoring retinal morphologic and functional changes in mice following optic nerve crush. Invest Ophthalmol Vis Sci. 2014;55:3766–74.
23. Munguba GC, Galeb S, Liu Y, Landy DC, Lam D, Camp A, et al. Nerve fiber layer thinning lags retinal ganglion cell density following crush axonopathy. Invest Ophthalmol Vis Sci. 2014;55:6505–13.
24. Rovere G, Nadal-Nicolás FM, Agudo-Barriuso M, Sobrado-Calvo P, Nieto-López L, Nucci C, et al. Comparison of retinal nerve fiber layer thinning and retinal ganglion cell loss after optic nerve transection in adult albino rats. Invest Ophthalmol Vis Sci. 2015;56:4487–98.
25. Nadal-Nicolás FM, Vidal-Sanz M, Agudo-Barriuso M. The aging rat retina: from function to anatomy. Neurobiol Aging. 2018;61:146–68.
26. Jeon CJ, Strettoi E, Masland RH. The major cell populations of the mouse retina. J Neurosci. 1998;18:8936–46.
27. Szél A, Röhlich P. Two cone types of rat retina detected by anti-visual pigment antibodies. Exp Eye Res. 1992;55:47–52.
28. Cull G, Cioffi GA, Dong J, Homer L, Wang L. Estimating normal optic nerve axon numbers in non-human primate eyes. J Glaucoma. 2003;12:301–6.
29. Kim CB, Tom BW, Spear PD. Effects of aging on the densities, numbers, and sizes of retinal ganglion cells in rhesus monkey. Neurobiol Aging. 1996;17:431–8.
30. Jonas JB, Müller-Bergh JA, Schlötzer-Schrehardt UM, Naumann GO. Histomorphometry of the human optic nerve. Invest Ophthalmol Vis Sci. 1990;31:736–44.
31. Kryger Z, Galli-Resta L, Jacobs GH, Reese BE. The topography of rod and cone photoreceptors in the retina of the ground squirrel. Vis Neurosci. 1998;15:685–91.
32. Merriman DK, Sajdak BS, Li W, Jones BW. Seasonal and post-trauma remodeling in cone-dominant ground squirrel retina. Exp Eye Res. 2016;150:90–105.
33. Li W. Ground squirrel - A cool model for a bright vision. Semin Cell Dev Biol. 2020;106:127–34.
34. Jacobs GH. The distribution and nature of colour vision among the mammals. Biol Rev Camb Philos Soc. 1993;68:413–71.
35. Marshak DW, Mills SL. Short-wavelength cone-opponent retinal ganglion cells in mammals. Vis Neurosci. 2014;31:165–75.
36. Nadal-Nicolás FM, Kunze VP, Ball JM, Peng BT, Krishnan A, Zhou G, et al. True S-cones are concentrated in the ventral mouse retina and wired for color detection in the upper visual field. Elife. 2020;9:56840.
37. Ortín-Martínez A, Jiménez-López M, Nadal-Nicolás FM, Salinas-Navarro M, Alarcón-Martínez L, Sauvé Y, et al. Automated quantification and topographical distribution of the whole population of S- and L-cones in adult albino and pigmented rats. Invest Ophthalmol Vis Sci. 2010;51:3171–83.
38. Ortín-Martínez A, Nadal-Nicolás FM, Jiménez-López M, Alburquerque-Béjar JJ, Nieto-López L, García-Ayuso D, et al. Number and distribution of mouse retinal cone photoreceptors: differences between an albino (Swiss) and a pigmented (C57/BL6) strain. PLoS ONE. 2014;9:e102392.
39. Jacobs GH, Neitz M, Deegan JF, Neitz J. Trichromatic colour vision in New World monkeys. Nature. 1996;382:156–8.
40. Nathans J, Thomas D, Hogness DS. Molecular genetics of human color vision: the genes encoding blue, green, and red pigments. Science. 1986;232:193–202.
41. Yokoyama S, Yokoyama R. Molecular evolution of human visual pigment genes. Mol Biol Evol. 1989;6:186–97.
42. Finlay BL, Franco ECS, Yamada ES, Crowley JC, Parsons M, Muniz JAPC, et al. Number and topography of cones, rods and optic nerve axons in New and Old World primates. Vis Neurosci. 2008;25:289–99.
43. Van Hooser SD, Nelson SB. The squirrel as a rodent model of the human visual system. Vis Neurosci. 2006;23:765–78.
44. Andrews MT. Advances in molecular biology of hibernation in mammals. Bioessays. 2007;29:431–40.
45. Staples JF. Metabolic flexibility: hibernation, torpor, and estivation. Compr Physiol. 2016;6:737–71.
46. Ou J, Ball JM, Luan Y, Zhao T, Miyagishima KJ, Xu Y, et al. iPSCs from a Hibernator provide a platform for studying cold adaptation and its potential medical applications. Cell. 2018;173:851–63.
47. Luan Y, Ou J, Kunze VP, Qiao F, Wang Y, Wei L, et al. Integrated transcriptomic and metabolomic analysis reveals adaptive changes of hibernating retinas. J Cell Physiol. 2018;233:1434–45.
48. Long KO, Fisher SK. The distributions of photoreceptors and ganglion cells in the California ground squirrel, Spermophilus beecheyi. J Comp Neurol. 1983;221:329–40.
49. Johnson PT, Geller SF, Reese BE. Distribution, size and number of axons in the optic pathway of ground squirrels. Exp Brain Res. 1998;118:93–104.

50. Merriman DK, Lahvis G, Jooss M, Gesicki JA, Schill K. Current practices in a captive breeding colony of 13-lined ground squirrels (Ictidomys tridecemlineatus). Lab Anim (NY). 2012;41:315–25.

51. Nadal-Nicolás FM, Salinas-Navarro M, Vidal-Sanz M, Agudo-Barriuso M. Two methods to trace retinal ganglion cells with fluorogold: from the intact optic nerve or by stereotactic injection into the optic tract. Exp Eye Res. 2015;131:12–19.

52. Jospeh SA, Knigge KA, Kalejs LM, Hoffman RA, Reid P. A stereotaxic atlas of the brain of the 13-line ground squirrel (citellus tridecemlineatus). Rochester Univ, NY: Dept of Anatomy; 1966.

53. Vaidya PG. A comparative study of the visual system in the diurnal ground squirrel, Citellus tridecemlineatus tridecemlineatus and in the nocturnal guinea pig, Cavia cobaya. Z Anat Entwicklungsgesch. 1965;124:505–21.

54. Kwong JMK, Caprioli J, Piri N. RNA binding protein with multiple splicing: a new marker for retinal ganglion cells. Invest Ophthalmol Vis Sci. 2010;51:1052–8.

55. Rodriguez AR, de Sevilla Müller LP, Brecha NC. The RNA binding protein RBPMS is a selective marker of ganglion cells in the mammalian retina. J Comp Neurol. 2014;522:1411–43.

56. Famiglietti EV, Sharpe SJ. Regional topography of rod and immunocytochemically characterized "blue" and "green" cone photoreceptors in rabbit retina. Vis Neurosci. 1995;12:1151–75.

57. Sánchez-Migallón MC, Valiente-Soriano FJ, Salinas-Navarro M, Nadal-Nicolás FM, Jiménez-López M, Vidal-Sanz M, et al. Nerve fibre layer degeneration and retinal ganglion cell loss long term after optic nerve crush or transection in adult mice. Exp Eye Res. 2018;170:40–50.

58. Sánchez-Migallón MC, Valiente-Soriano FJ, Nadal-Nicolás FM, Vidal-Sanz M, Agudo-Barriuso M. Apoptotic retinal ganglion cell death after optic nerve transection or crush in mice: delayed RGC loss with BDNF or a Caspase 3 Inhibitor. Invest Ophthalmol Vis Sci. 2016;57:81–93.

59. Rodriguez-Ramos Fernandez J, Dubielzig RR. Ocular comparative anatomy of the family Rodentia. Vet Ophthalmol. 2013;16:94–9.

60. Pasteels B, Rogers J, Blachier F, Pochet R. Calbindin and calretinin localization in retina from different species. Vis Neurosci. 1990;5:1–16.

61. Sun D, Lye-Barthel M, Masland RH, Jakobs TC. The morphology and spatial arrangement of astrocytes in the optic nerve head of the mouse. J Comp Neurol. 2009;516:1–19.

62. Nadal-Nicolás FM, Jiménez-López M, Salinas-Navarro M, Sobrado-Calvo P, Alburquerque-Béjar JJ, Vidal-Sanz M, et al. Whole number, distribution and co-expression of brn3 transcription factors in retinal ganglion cells of adult albino and pigmented rats. PLoS ONE. 2012;7:e49830.

63. Zhang Y, Zhang S, Xia Y, Ji Y, Jiang W, Liet M, et al. In vivo evaluation of retinal ganglion cells and optic nerve's integrity in large animals by multi-modality analysis. Exp Eye Res. 2020;197:108117.

64. Levkovitch-Verbin H, Quigley HA, Kerrigan-Baumrind LA, D'Anna SA, Kerrigan D, Pease ME. Optic nerve transection in monkeys may result in secondary degeneration of retinal ganglion cells. Invest Ophthalmol Vis Sci. 2001;42:975–82.

65. Abreu M, Kicliter E, Lugo-Garcia N. Displaced amacrine cells in the ganglion cell layer of the ground squirrel retina. P R Health Sci J. 1993;12:137–41.

66. Wässle H, Grünert U, Röhrenbeck J, Boycott BB. Cortical magnification factor and the ganglion cell density of the primate retina. Nature. 1989;341:643–6.

67. Wässle H, Grünert U, Röhrenbeck J, Boycott BB. Retinal ganglion cell density and cortical magnification factor in the primate. Vision Res. 1990;30:1897–911.

68. Curcio CA, Allen KA. Topography of ganglion cells in human retina. J Comp Neurol. 1990;300:5–25.

69. Mariani AP, Hersh LB. Synaptic organization of cholinergic amacrine cells in the rhesus monkey retina. J Comp Neurol. 1988;267:269–80.

70. Cepko CL, Austin CP, Yang X, Alexiades M, Ezzeddine D. Cell fate determination in the vertebrate retina. Proc Natl Acad Sci U.S.A. 1996;93:589–95.

71. Livesey FJ, Cepko CL. Vertebrate neural cell-fate determination: lessons from the retina. Nat Rev Neurosci. 2001;2:109–18.

72. Kisseleff E, Vigouroux RJ, Hottin C, Lourdel S, Shah P, Chédotal A, et al. Glycogen Synthase Kinase 3 Regulates the Genesis of the Rare Displaced Ganglion Cell Retinal Subtype. Preprint at https://doi.org/10.1101/2021.01.06.425300 (2021).

73. Johnson KP, Fitzpatrick MJ, Zhao L, Wang B, McCracken S, Williams PR, et al. Cell-type-specific binocular vision guides predation in mice. Neuron. 2021;109:1527–39.

74. Levkovitch-Verbin H, Quigley HA, Martin KRG, Zack DJ, Pease ME, Valenta DF. A model to study differences between primary and secondary degeneration of retinal ganglion cells in rats by partial optic nerve transection. Invest Ophthalmol Vis Sci. 2003;44:3388–93.

75. Khakh BS, Sofroniew MV. Diversity of astrocyte functions and phenotypes in neural circuits. Nat Neurosci. 2015;18:942–52.

76. Zai LJ, Wrathall JR. Cell proliferation and replacement following contusive spinal cord injury. Glia. 2005;50:247–57.

77. Yang T, Dai Y, Chen G, Cui S. Dissecting the dual role of the glial scar and scar-forming astrocytes in spinal cord injury. Front Cell Neurosci. 2020;14:78.

78. Greenhalgh AD, David S. Differences in the phagocytic response of microglia and peripheral macrophages after spinal cord injury and its effects on cell death. J Neurosci. 2014;34:6316–22.

79. Shinozaki Y, Shibata K, Yoshida K, Shigetomi E, Gachet C, Ikenaka K, et al. Transformation of astrocytes to a neuroprotective phenotype by microglia via P2Y1 receptor downregulation. Cell Rep. 2017;19:1151–64.

80. Anderson MA, Burda JE, Ren Y, Ao Y, O'Shea TM, Kawaguchiet R, et al. Astrocyte scar formation aids central nervous system axon regeneration. Nature. 2016;532:195–200.

81. Gu Y, Cheng X, Huang X, Yuan Y, Qin S, Tan Z, et al. Conditional ablation of reactive astrocytes to dissect their roles in spinal cord injury and repair. Brain Behav Immun. 2019;80:394–405.

82. Sugar O, Gerard RW. SPINAL CORD REGENERATION IN THE RAT. J Neurophysiol. 1940;3:1–19.

83. Clemente CD, Windle WF. Regeneration of severed nerve fibers in the spinal cord of the adult cat. J Comp Neurol. 1954;101:691–731.

84. Yiu G, He Z. Glial inhibition of CNS axon regeneration. Nat Rev Neurosci. 2006;7:617–27.

85. Ramírez AI, Salazar JJ, de Hoz R, Rojas B, Gallego BI, Salinas-Navarro M, et al. Quantification of the effect of different levels of IOP in the astroglia of the rat retina ipsilateral and contralateral to experimental glaucoma. Invest Ophthalmol Vis Sci. 2010;51:5690–6.

86. de Hoz R, Gallego BI, Ramírez AI, Rojas B, Salazar JJ, Valiente-Soriano FJ, et al. Rod-like microglia are restricted to eyes with laser-induced ocular hypertension but absent from the microglial changes in the contralateral untreated eye. PLoS ONE. 2013;8:e83733.

87. Rojas B, Gallego BI, Ramírez AI, Salazar JJ, de Hoz R, Valiente-Soriano FJ, et al. Microglia in mouse retina contralateral to experimental glaucoma exhibit multiple signs of activation in all retinal layers. J Neuroinflammation. 2014;11:133.

88. Osborne NN, Li G-Y, Ji D, Mortiboys HJ, Jackson S. Light affects mitochondria to cause apoptosis to cultured cells: possible relevance to ganglion cell death in certain optic neuropathies. J Neurochem. 2008;105:2013–28.

89. Osborne NN, Núñez-Álvarez C, Del Olmo-Aguado S, Merrayo-Lloves J. Visual light effects on mitochondria: the potential implications in relation to glaucoma. Mitochondrion. 2017;36:29–35.

90. Guttenplan KA, Stafford BK, El-Danaf RN, et al. Neurotoxic reactive astrocytes drive neuronal death after retinal injury. Cell Rep. 2020;31:107776.

AUTHOR CONTRIBUTIONS
The experiments were conceived and designed by FMNN and WL. Experiments were conducted by FMNN, XX, TZ, KJM, SC, and data were analyzed by FMNN, XX, KJM, WL. The automatic scripts were written by FMNN. Visualization by FMNN and WL. The original draft was written by FMNN and WL and all authors have written, reviewed and edited the final paper.

ETHICS APPROVAL AND CONSENT TO PARTICIPATE

Each species was treated and maintained according to their unique protocols (mouse, ASP#606; TLGS: ASP#595) approved by the National Institutes of Health guidelines for Animal Care and Use Committee in research and by the Ethical and Animal Studies Committee of the National Eye Institute. All animal studies conformed to the Statement for the Use of Animals in Ophthalmic and Vision research of the Association for Research in Vision and Ophthalmology (ARVO). In conducting this research, we adhered to the laws of the United States and regulations of the US Department of Agriculture.

COMPETING INTERESTS

The authors declare no competing interests.